Editors' Suggestion

Single-particle tunneling spectroscopy and superconducting gaps in the layered iron-based superconductor $KCa_2Fe_4As_4F_2$

Wen Duan,[1] Kailun Chen,[1] Wenshan Hong,[2,3] Xiaoyu Chen,[1] Huan Yang,[1,*] Shiliang Li,[2,3,4] Huiqian Luo,[2,4] and Hai-Hu Wen[1,†]

[1]*National Laboratory of Solid State Microstructures and Department of Physics, Collaborative Innovation Center of Advanced Microstructures, Nanjing University, Nanjing 210093, China*

[2]*Beijing National Laboratory for Condensed Matter Physics, Institute of Physics, Chinese Academy of Sciences, Beijing 100190, China*

[3]*School of Physical Sciences, University of Chinese Academy of Sciences, Beijing 100190, China*

[4]*Songshan Lake Materials Laboratory, Dongguan, Guangdong 523808, China*

(Received 4 February 2021; accepted 1 June 2021; published 23 June 2021)

We perform a scanning tunneling microscopy/spectroscopy study on the layered iron-based superconductor $KCa_2Fe_4As_4F_2$ with a critical temperature of about 33.5 K. Two types of terminated surfaces are generally observed after cleaving the samples in vacuum. On one commonly obtained surface, we observe a full gap feature with energy gap values close to 4.6 meV. This type of spectrum shows a clean and uniform full gap in space, which indicates the absence of gap nodes in this superconductor. Quasiparticle interference patterns have also been measured which show an intraband scattering pattern possibly due to the holelike α pocket. The Fermi energy of this band is only about 24 ± 6 meV, as derived from the energy dispersion result. Meanwhile, impurity-induced bound-state peaks can be observed at about ± 2.2 meV on some spectra, and the peak value seems to be independent of magnetic field. On the second type of surface, which is rarely obtained, the fully gapped feature can still be observed in the tunneling spectra, although multiple gaps are obtained from either a single spectrum or separate ones, and the gap values determined from coherence peaks locate mainly in the range from 4 to 7 meV. Our results clearly indicate the multiple and nodeless superconducting gap nature of the layered superconductor $KCa_2Fe_4As_4F_2$, and the superfluid is mainly contributed by the holelike Fermi surfaces near the Γ point. This result should inspire further consideration of the effect of the shallow and incipient bands near the M point and help us to understand the pairing mechanism in this highly layered iron-based superconductor.

DOI: 10.1103/PhysRevB.103.214518

I. INTRODUCTION

Iron-based superconductors (FeSCs) are the second family of unconventional high-temperature superconductors. In most FeSCs, several Fe derivative d bands cross the Fermi energy, forming the electron- and holelike pockets. Meanwhile, band structures and Fermi surfaces are quite different in various FeSCs, and they are also very sensitive to chemical doping or external pressure. The widely accepted $s^{\pm}$ pairing symmetry in some FeSCs is based on the nesting between hole pockets near the Γ point and electron pockets around the M point with similar sizes in the weak-coupling scenario, but the gap symmetry and the gap structure can be different in other FeSCs because of different structures of Fermi surfaces [1].

The newly found $ACa_2Fe_4As_4F_2$ (A = K, Rb, Cs) is a representative compound of the layered FeSCs, and the critical temperature T_c ranges from 28 to 33 K [2–4]. The crystal structure of $KCa_2Fe_4As_4F_2$ (K12442) is shown in Fig. 1(a) as an example; one can see that in these materials, double FeAs layers are separated by insulating Ca_2F_2 layers. Such a layered structure results in significant anisotropy of superconductivity and normal-state resistance [4–7]. It is supposed that the 12442-type FeSCs have intrinsic hole conduction with a doping level of 0.25 hole/Fe. Interestingly, it is easy to transform the primary carrier from p type to n type by Co or Ni doping, but T_c decreases with the increase of the doped concentration of Co or Ni dopants [8,9]. Meanwhile, T_c can be slightly enhanced by applying a hydrostatic pressure [10]. Transport measurements in K12442 single crystals suggest that the in-plane upper critical field is dominated by the Pauli paramagnetic effect instead of the orbital effect [11]. Theoretical calculation predicts that there are several hole and electron pockets in K12442 [8,12,13]. Based on recent angle-resolved photoemission spectroscopy (ARPES) work conducted on K12442, three separate hole pockets, α, β, and γ, are observed around the Γ point, and one tiny electron pocket and four incipient hole bands (which barely touch the Fermi energy) are observed around the M point [14]. Obviously, this topology of the Fermi surface cannot satisfy the nesting condition because of the very different sizes of hole and electron pockets. The nesting condition is satisfied by Co doping to K12442 with a doping level of about 0.1, but T_c decreases to about 25 K [8]. In this point of view, the superconductivity in 12442-type FeSCs may be different

*huanyang@nju.edu.cn
†hhwen@nju.edu.cn

 ©2021 American Physical Society

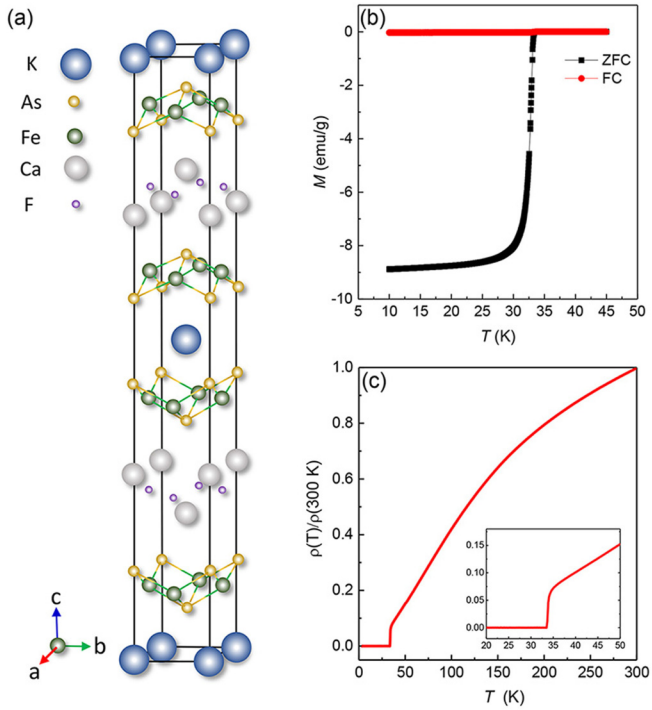

FIG. 1. (a) Crystal structure of $KCa_2Fe_4As_4F_2$. (b) Temperature-dependent magnetization measured in zero-field-cooled (ZFC) and field-cooled (FC) processes under a magnetic field of 10 Oe. (c) Temperature dependence of normalized in-plane resistance measured at 0 T.

from that of other FeSCs. ARPES measurements in K12442 exhibit six nodeless gaps with gap values ranging from 2 to 8 meV for different Fermi pockets. The multiple and nodeless gap features are also proved by different experimental methods [15,16]. However, some other works claim that there might be line nodes on the superconducting gap(s) in 12442-type FeSCs [17–19]. The controversies over the existence of gap nodes in the 12442 system require further investigation. Although the nesting condition is not satisfied in 12442-tpye FeSCs, the spin resonance peak is still observed around $Q = (0.5, 0.5)$ [20,21], which corresponds to the scattering vector from the hole to electron pockets. Here the $s^{\pm}$ pairing symmetry with the spin resonance can be explained in the strong-coupling approach with the absence of the nesting condition [22]. In addition, the spin resonance mode with a downward dispersion is observed in K12442, and this kind of dispersion is similar to the behavior in cuprates [20].

In this paper, we report the experimental study of $KCa_2Fe_4As_4F_2$ single crystals by scanning tunneling microscopy/spectroscopy (STM/STS). The fully gapped feature is observed in almost all tunneling spectra. We also conduct quasiparticle interference (QPI) measurements of the sample in order to obtain information about the Fermi pockets. Our results provide fruitful information on this multiband superconductor.

II. EXPERIMENTAL METHODS

The $KCa_2Fe_4As_4F_2$ single crystals used in this work were grown by the self-flux method [4]. Temperature-dependent magnetization and normalized resistance are shown in Figs. 1(b) and 1(c), and both of them show fine superconducting transitions with critical temperature T_c of about 33.5 K determined from the zero resistance. STM/STS measurements were carried out using a scanning tunneling microscope (USM-1300, Unisoku Co., Ltd.). The K12442 samples were cleaved at about 77 K in ultrahigh vacuum with a base pressure of about 1×10^{-10} Torr, and then they were transferred to the microscopy head, which was kept at a low temperature. Electrochemically etched tungsten tips were used for STM/STS measurements after cleaning by electron-beam heating. A typical lock-in technique was used in tunneling spectrum measurements with an ac modulation of 0.1 mV (0-peak value) and a frequency of 931.773 Hz. Voltage offsets were carefully calibrated before STS measurements.

III. RESULTS

A. Topography and tunneling spectra

Figure 2(a) shows a typical topographic image measured on the surface of a K12442 single crystal. Based on the lattice structure of K12442, there are layers of alkali-metal K atoms and of alkaline-earth-metal Ca atoms. The cleavage may occur in these layers with relatively weak bonding energy. After the cleavage, most likely, half of the K or Ca atoms remain in the surface layer of each separated part, which makes both surface unpolarized. Proof can be seen in the atomically resolved topography shown in the top right inset in Fig. 2(a) measured on a flat area far away from any defects. The topography shows a square lattice with a lattice constant of about 5.3 Å, which is approximately equal to $\sqrt{2}$ times the K-K or Ca-Ca lattice constant ($a_0 = 3.87$ Å). From the topographic image, one can see that there are many hollows with different sizes on the flat background. The depths of the hollows are from 100 to 300 pm, and these hollows can be clearly seen in the rescanned image shown in the bottom left inset in Fig. 2(a). Similar kinds of hollows have been observed in $NaFe_{1-x}Co_xAs$ [23], LiFeAs [24], and $RbFe_2As_2$ [25] but with much lower densities, and they may be the assembled vacancies of alkali-metal atoms on the reconstructed surface. In Fig. 2(b), we show a typical tunneling spectrum on the surface measured in a wide energy window. The differential conductance is much larger on the negative-bias side than that on the positive-bias side, which is consistent with the asymmetric density of states (DOS) from previous band calculation results [12,13].

Figure 2(c) shows two tunneling spectra measured at the two marked positions in the bottom left inset in Fig. 2(a); that is, one is measured at a position in a hollow, and the other is measured at a position in the flat area far away from the hollows. One can see that the two spectra show almost the same feature, which suggests that hollows have very little influence on the superconductivity. A slight suppression of the intensity of coherence peaks can be observed on the spectrum measured in the hollow compared to that measured in the flat area. Both spectra show a full gap feature with a pair of coherence peaks located at energies of about ±4.6 meV. Then we carry out the Dynes model [26] with an *s*-wave gap to fit the spectrum measured in the flat area. The fitting result is shown as the green curve in Fig. 2(c) by using an isotropic *s*-wave gap

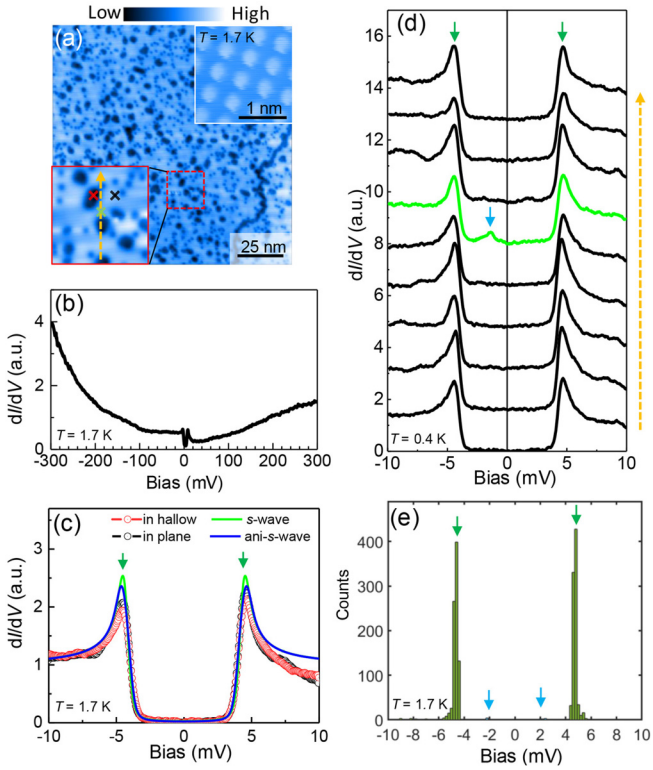

FIG. 2. (a) A typical topographic image taken on a surface of K12442 measured at $T = 1.7$ K with set point conditions of $V_{set} = 20$ mV and $I_{set} = 200$ pA. The inset in the bottom left corner shows a rescanned image with higher resolution of the area marked by the red dashed square. The inset in the top right corner shows the atomically resolved topography measured in another flat area ($V_{set} = 10$ mV, and $I_{set} = 500$ pA). (b) A typical tunneling spectrum measured in an energy window far beyond the superconducting gap ($V_{set} = 300$ mV, and $I_{set} = 500$ pA). (c) Two tunneling spectra measured at the marked positions by the red and black crosses in the bottom left inset in (a) ($V_{set} = 10$ mV, and $I_{set} = 200$ pA). The solid lines show fitting results by the Dynes model with isotropic and slightly anisotropic s-wave gaps. (d) Spatially resolved tunneling spectra measured along the yellow dashed line in the bottom left inset in (a) ($V_{set} = 20$ mV, and $I_{set} = 200$ pA). The green spectrum is measured at the center of the green cross shown in the bottom left inset in (a), which exhibits a peak at bias voltage of about -2 mV (marked by a blue arrow), and it may be the impurity-induced state. (e) The statistics of peak energies in 845 tunneling spectra measured at randomly selected points in the area of (a) ($V_{set} = 10$ mV, and $I_{set} = 200$ pA).

$\Delta(\theta) = 4.3$ meV and the scattering rate $\Gamma = 0.12$ meV. Obviously, the coherence peak is too sharp for the fitting curve, so slight anisotropy is required for the gap function. The best fitting result is shown by the blue curve in Fig. 2(c), and the gap function reads $\Delta(\theta) = 4.6(0.93 + 0.07\cos 2\theta)$ meV, with $\Gamma = 0.1$ meV. Here the gap maximum Δ_{max} is close to the energy value of coherence peaks, and it is also similar to gap values of hole pockets of α and β_1 or the electron pocket of δ from the ARPES measurements [14]. We also measure a set of tunneling spectra along the dashed line in the bottom left inset in Fig. 2(a), and the spectra are shown in Fig. 2(d). All the spectra are homogeneous except for a slight change in the coherence peak energy. On the green spectrum in Fig. 2(d), one can see that there is a small peak at about -2 mV marked by the blue arrow. It should be noted that this spectrum is not measured in the hollow, and there is no unique feature on the topography. The peak is likely to be the bound state induced by an impurity underneath the surface, which will be discussed in Sec. III C. We then conduct the tunneling spectrum measurement over the whole area in Fig. 2(a) and calculate the statistics of peak energies on 845 measured spectra. The result is shown in Fig. 2(e). The coherence peaks are located mostly from 4.4 to 5.4 meV from the statistics. About 2% of spectra have low-energy peaks within an energy range of $\pm(2.2 \pm 0.4)$ meV; they can appear either at the hollow positions or in the flat area.

B. Results of quasiparticle interference

QPI measurements and the related analysis are very useful because they can provide information about the Fermi surface [27], the gap anisotropy [28,29], and the gap signs [30–34] in a superconductor. We also measure the differential conductance mapping and show a QPI mapping at $E = 10$ meV in Fig. 3(b). Although the hollows in the topography do not affect the superconductivity too much, standing waves can clearly be seen surrounding these hollows. When we carry out the Fourier transformation to the QPI mapping, we can obtain the Fourier-transformed (FT) QPI pattern and show it in Fig. 3(d). In K12442, a previous ARPES study [14] observed three hole pockets (α, β, and γ) around the Γ point and one tiny electron δ pocket around the M point. We plot a sketch map of Fermi surfaces in Fig. 3(c). Here the intraband scattering should locate around the center point of the FT-QPI pattern shown in Fig. 3(d), and the simulated scattering results between the hole and the electron pockets are plotted as the four gray patterns in Fig. 3(f). However, these scattering patterns are not observed in the experimental data shown in Fig. 3(d). They are more clear in the linecut intensity of the differential conductance shown in Fig. 3(e). One can see that the line profile plot of the differential conductance is almost featureless near the points $q = \pm\sqrt{2}\pi/a_0$ which connect the Γ and M points in momentum space. The absence of the characteristic scattering patterns between the hole and electron pockets may be explained by following two possible reasons: (a) a low DOS at the Fermi energy for the small electron δ pockets and (b) the unsensitive tunneling matrix element effect, as a result of which we cannot detect the electron δ pocket.

Since we have not observed the scattering between the hole and electron pockets, we try to get some information about the intraband scattering from the QPI data in a large area. Results of QPI mappings and corresponding FT-QPI patterns are shown in Fig. 4. At zero energy, almost no clear features can be observed in the QPI pattern in Fig. 4(b), which is consistent with the full gap feature from tunneling spectrum measurements. At $E = \pm 2.3$ meV, one can obviously see in Fig. 4(c) that there are about 15 clear spots induced by the impurity bound state at this energy. When we go back to the topographic image in Fig. 4(a), we can conclude that there is no evident correlation between impurity locations and the hollows on the top surface. The impurity may be beneath the top surface, e.g., in the FeAs layer. In FT-QPI patterns,

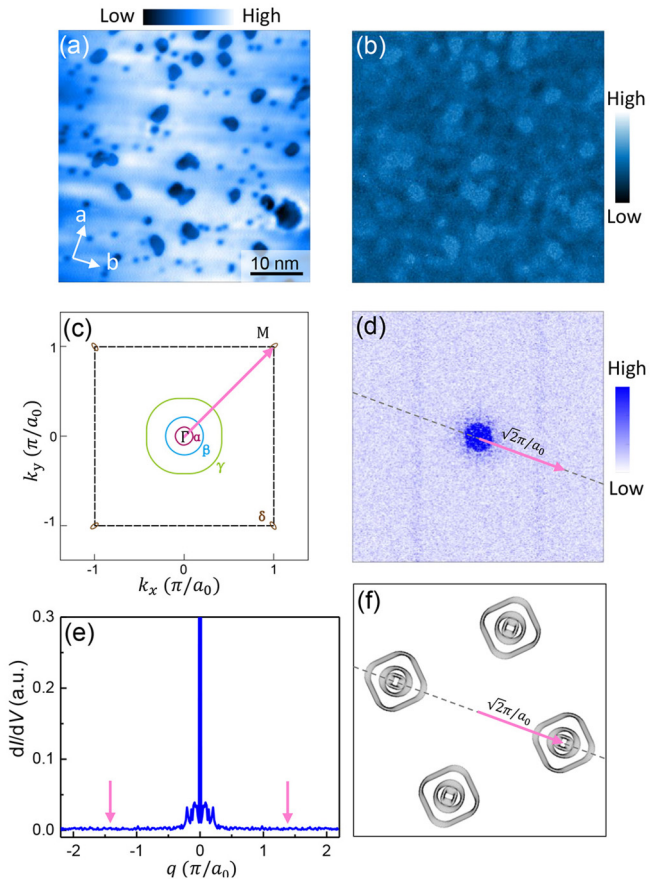

FIG. 3. (a) Topographic image and (b) the corresponding normal-state QPI mapping at $E = 10$ meV measured in the same area ($V_{set} = 30$ mV, $I_{set} = 200$ pA). (c) Schematic plot of Fermi surfaces derived from a previous ARPES study [14]. (d) The Fourier-transformed pattern of the QPI mapping in (b). (e) Line profile plot of the intensity of the FT-QPI pattern along the black dashed line in (d); the arrows indicate the position of scattering vectors connecting the Γ and M points. (f) The simulated scattering patterns between the hole and electron pockets plotted as gray patterns with a center of $\sqrt{2}\pi/a_0$ from the center of the FT-QPI pattern. Here the gray patterns are the selected patterns in the self-correlated image in (c). The arrow represents the scattering vector connecting the Γ and M points. Comparing (d) and (f), one can see that the scattering between hole and electron pockets has not been detected by our experimental data. All measurements are carried out at 0.7 K.

the scattering intensity reflects the joint DOS between two scattering points in **k** space on the Fermi surface [27]. Being consistent with the tunneling spectrum for a fully gapped superconductor, the FT-QPI pattern is almost featureless at $E = 0$ meV, and the intensity of the FT-QPI pattern is very strong near the coherence peak energy [28,29,35]. In K12442, the most frequent superconducting gap value or the coherence peak energy is about 4.6 meV from tunneling spectrum measurements on this surface; therefore, the intensity of FT-QPI patterns is very strong at $E = \pm 4.6$ meV. Although we cannot distinguish the detailed scattering features, it is clear that there are fourfold diamondlike patterns around the center in FT-QPI patterns. The traces of these outlines arising from the FT-QPI patterns are marked by orange dashed lines in Figs. 4(m)–4(o) and 4(q)–4(s). The sizes of such fourfold diamondlike patterns shrink with the increase of the energy, which can be clearly seen in the energy dispersion plot [Fig. 4(t)]. This result suggests that the scattering may be due to the intraband scattering of a hole pocket near Γ. We try to fit the dispersion data with a parabola, and the fitting result is shown in Fig. 4(t). Here we can obtain the band-top energy of 24 ± 6 meV from the peak value of the fitting curve. In addition, the fitting curve cuts the Fermi level at the points $q = \pm 0.18\pi/a_0$ in **q** space, and this radius corresponds to the diameter of the Fermi surface in which the intraband scattering happens [27]. As shown by a previous work [14], the holelike α pocket has the smallest diameter of about $0.2\pi/a_0$, and the band top of this pocket is about 40 meV from the band calculation. The values of the band top and the Fermi-pocket size determined from our experiments are both comparable to those from the previous ARPES work; therefore, the Fermi pocket associated with our QPI measurement is supposed to be the holelike α pocket.

C. Impurity bound states

In order to investigate low-energy peaks at about ±2.2 meV, we measure spatial evolution of tunneling spectra [Fig. 5(c)] along the arrowed line across two bright spots in the QPI mapping [Fig. 5(b)]. One can see in Fig. 5(c) that the tunneling spectra have a similar feature of peaks across these two spots. The coherence peaks are suppressed near impurities, which makes impurities behave as troughs in Figs. 4(d) and 4(h). It should be noted that impurity bound-state peaks show electron-hole asymmetry in Fig. 5(c). When we do statistics to 15 impurities marked by circles in Fig. 4(c), the QPI intensity $g(E)$ at the impurity center has a stronger amplitude for all the impurities in the image taken at $E = -2.3$ meV than that taken at $E = 2.3$ meV. The averaged ratio $g(E = -2.3\ \text{meV})/g(E = 2.3\ \text{meV}) = 1.36 \pm 0.25$, which is derived at the centers of these 15 impurities. QPI mappings behave very differently in real space, as shown in Figs. 4(d) and 4(h) when compared with those in Figs. 4(c) and 4(g): a lot of standing waves in Figs. 4(d) and 4(h) are absent in Figs. 4(c) and 4(g). These standing waves result in the fourfold diamondlike patterns in FT-QPI patterns, but they are not structured around the impurities which behave as troughs in Figs. 4(d) and 4(h). The Fermi surface should still be gapped in most areas far from impurities at $E = \pm 2.3$ meV based on the tunneling spectra shown in Fig. 2(c). In addition, the FT-QPI patterns measured at $E = \pm 2.3$ meV do not have clear outer contours, which is different from the features in FT-QPI patterns measured at higher energies. Based on the analysis of impurity images with the enlarged view shown in the insets of Figs. 4(l) and 4(p), the patterns in Figs. 4(l) and 4(p) are derived from the FT result to the real-space image of these impurities instead of the intraband scattering of the Fermi surface. The average size of impurities imaged at $E = 2.3$ meV is larger than that of impurities imaged at $E = -2.3$ meV, and the ratio of the full width at half maximum (FWHM) is FWHM($E = 2.3$ meV)/FWHM($E = -2.3$ meV) $= 1.37 \pm 0.29$. This ratio is consistent with the inverse radius ratio of the central disk shown in Figs. 4(l) and 4(p). Such impurity bound-state peaks can be even sharper at 0.4 K, and one example can be seen in Fig. 6(a). The

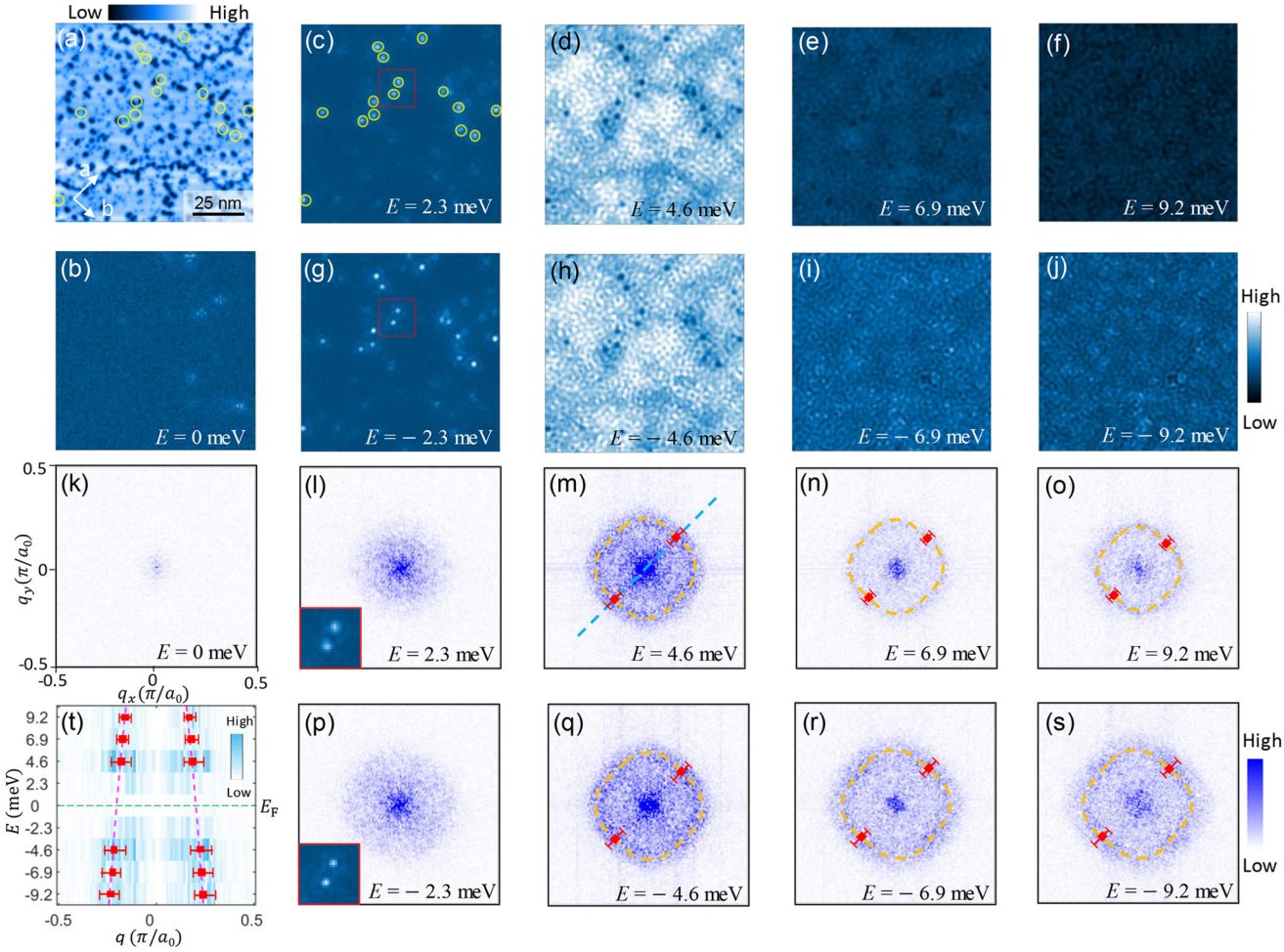

FIG. 4. (a) Large-scale topographic image measured on the surface of K12442. (b)–(j) The QPI mapping measured in (a) at different energies with $B = 0$ T and $T = 1.1$ K ($V_{set} = 10$ mV, $I_{set} = 200$ pA). Circles in (a) and (c) mark positions of impurities with the bound-state energy at about ± 2.3 mV. The locations of these impurities seem to be irrelevant to the hollows on the top surface. (k)–(s) Corresponding FT-QPI patterns derived from Fourier transformation to the QPI mappings in (b)–(j), respectively. The insets in (l) and (p) show enlarged views of two impurities framed by squares in (c) and (g), respectively. (t) The energy dispersion of intensity in FT-QPI patterns along the diagonal direction marked by the blue dashed line in (m). Before the patterns were plotted, a two-dimensional Gaussian function background was subtracted in the center of all the FT-QPI patterns with a full width at half maximum about $0.18\pi/a_0$. Red solid squares represent the sizes of the FT-QPI patterns marked as orange dashed circles in (m)–(o) and (q)–(s). The error bars highlighted in (t) reflect roughly the estimated width of the circlelike outline of the FT-QPI pattern. The energy dispersion feature seems to be holelike. The dashed curve is a fitting curve to the red solid squares by a parabolic equation, and we can obtain energy $E_b \approx 24 \pm 6$ meV for the top of the band.

spectrum feature near zero bias can even be affected by these low-energy peaks. The extremely sharp peaks may exclude the possibility of a smaller superconducting gap because we cannot fit the experimental data well using the Dynes model with two superconducting gaps. In addition, the peaks at about ± 2 meV disappear when the temperature is 8 K, but the coherence peaks at about ± 5 meV can exist at temperatures above 15 K. Following the discussion above, we argue that low-energy peaks are impurity-induced bound states, although these impurities locate underneath the top layer. In Fig. 6(c), we show tunneling spectra measured at the center of a bright spot and under different magnetic fields. The amplitude of the impurity-induced peak decreases with the increase of the magnetic field. The inset in Fig. 6(c) shows an enlarged view of the impurity-induced peak on the negative-energy side, and the peak energy is almost unchanged under a magnetic field of 4 T. From a previous report, the field-induced peak-shift slope is about 0.06 meV/T for the impurity bound state induced by a magnetic Fe-vacancy impurity with a Landé factor $g = 2$ [36]. Based on this slope, we can calculate the energy shift is about 0.24 meV when the field changes from 0 to 4 T. However, the energy shift is negligible for the impurity bound state in the K12442 sample; we can argue that the impurity may be nonmagnetic or weakly magnetic. In addition, the peak feature is similar to the bound-state peak of the As vacancy [37], so impurities are likely to be nonmagnetic As vacancies in the FeAs layer underneath.

D. Tunneling spectra measured on another kind of terminated surface

In the K12442 sample, we also observe other areas with different topographic features, and one example is shown in Fig. 7(a). This kind of surface is rarely observed, with

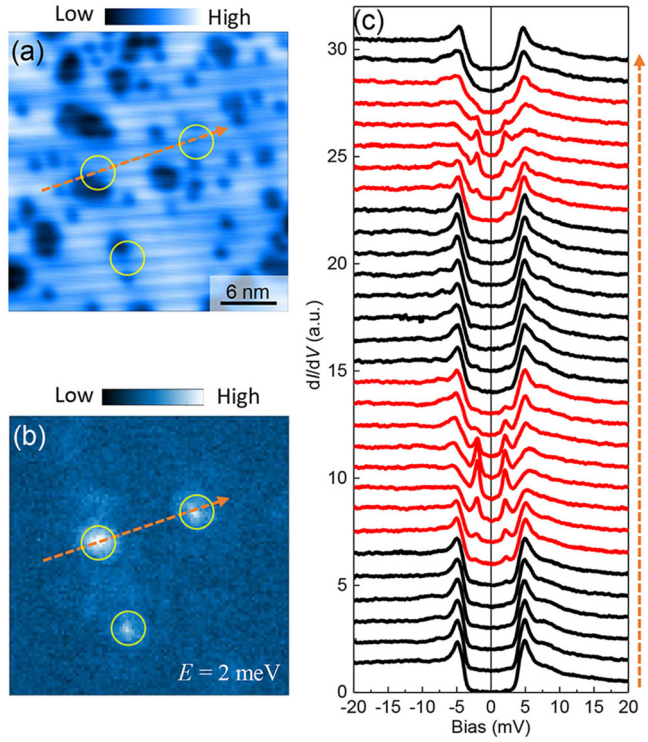

FIG. 5. (a) Topographic image ($V_{set} = 20$ mV, $I_{set} = 200$ pA) and (b) QPI mapping at $E = 2$ meV ($V_{set} = 20$ mV, $I_{set} = 200$ pA) measured in the same area. One can see three bright spots in (b). (c) A set of tunneling spectra ($V_{set} = 20$ mV, $I_{set} = 200$ pA) measured along the arrowed line in (a) or (b) crossing the centers of these two spots. The tunneling spectra in red are the ones measured in the area of the bright spot. All measurements were carried out at 1.7 K.

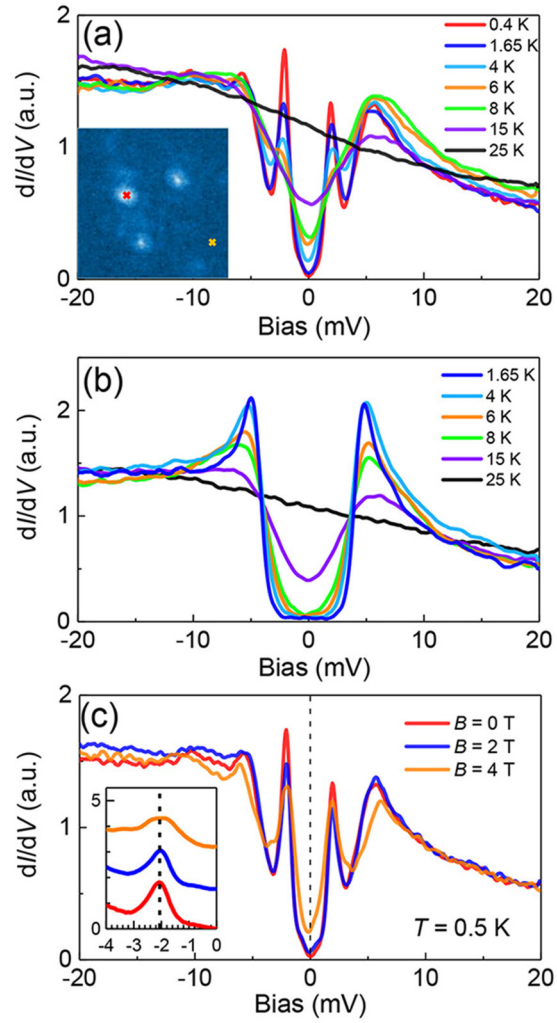

FIG. 6. Temperature-dependent evolution of the tunneling spectra measured (a) at the bright-spot center and (b) far away from any impurities. Specifically, (a) and (b) are measured at centers of the red and yellow crosses marked in the inset in (a), respectively. (c) Magnetic field evolution of the tunneling spectra measured at the impurity center. The inset shows an enlarged view of the bound-state peak at about −2 meV. Set point conditions: $V_{set} = 20$ mV, $I_{set} = 200$ pA.

a possibility of once in eight cleavage procedures. On this surface the hollows are much smaller than the ones shown in Fig. 2(a). However, from the atomically resolved surface shown in the inset in Fig. 7(a), the lattice constant is also about 5.3 Å, which is close to the value obtained in Fig. 2(a). Figure 7(b) shows a tunneling spectrum measured in a wide bias range. The spectrum has behavior similar to the one shown in Fig. 2(b): both show the particle-hole asymmetry. The quantitative difference between them is the considerable bias-voltage dependence of dI/dV on the negative-bias side of the spectrum shown in Fig. 7(b). This suggests slightly different band structures in these two kinds of surfaces. In the area in Fig. 7(a), we can detect spectra with different gap energies, and four examples are shown in Figs. 7(c)–7(f). In the spectrum shown in Fig. 7(f), we can also see low-energy peaks at about ±2.5 meV which may be attributed to the impurity-induced bound states. In addition, we can see that coherence peaks in spectra locate in a wider energy range than the ones shown in Fig. 2(d). In addition, hump features can be observed at energy near ±10 meV on some spectra. The humps in tunneling spectra may be a feature of a larger superconducting gap or may be the bosonic mode which has been observed in many FeSCs [38–40]. Figure 7(g) shows the energy statistic results for all the peak features based on 900 spectra measured in the area in Fig. 7(a). One can see that the coherence peak features are in the range of ±(4–7) meV with possible local maxima at about ±4.4, ±5.4, and ±6.2 meV. This suggests a multigap feature in the superconductor. The hump feature appears in a high energy range of ±(8–11) meV with the maximum probability at about ±9.8 meV.

Figure 8(a) shows a typical topography where a low-lying layer can be observed. The size of such an exposed low-lying area is dozens of nanometers, and the average height of this area is about 1 Å lower than the top surface. Then we measure the tunneling spectra across the exposed low-lying area and show them in Fig. 8(b). One can see that the fully gapped feature can be observed in all the spectra, but energy values of the coherence peaks shift from about ±6 meV on the top layer to about ±8 meV in the exposed low-lying area. The feature is clearer in the coherence peak energy mapping shown in Fig. 8(c) with a much larger coherence peak energy in the exposed low-lying area.

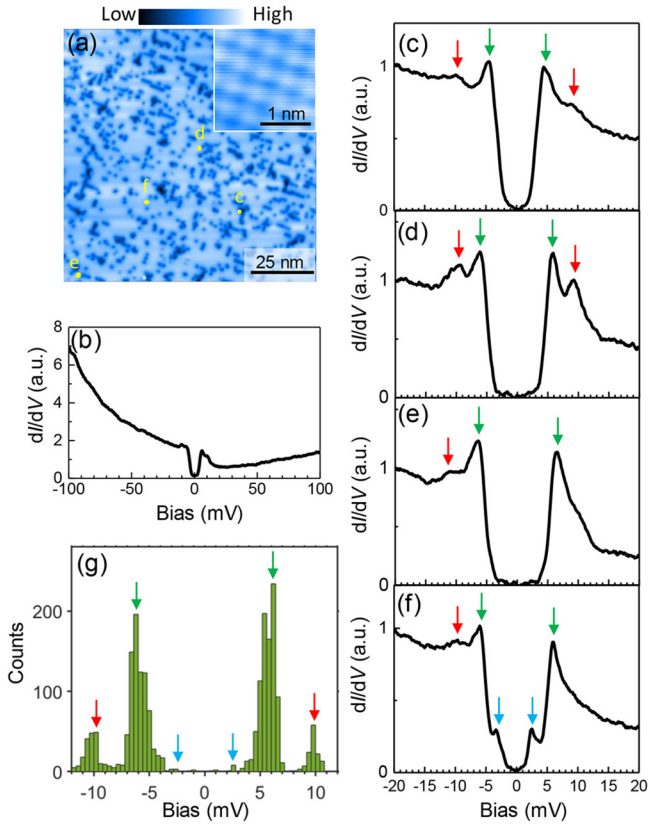

FIG. 7. (a) Topographic image of another kind of terminated surface ($V_{set} = 1$ V, $I_{set} = 20$ pA). Hollows in this topography have a lower density and a smaller averaged size when compared with ones in Fig. 2(a). The inset shows the atomically resolved topography measured in the flat area far away from hollows ($V_{set} = 100$ mV, $I_{set} = 200$ pA). (b) A typical tunneling spectrum measured to high energy ($V_{set} = 100$ mV, $I_{set} = 200$ pA). (c)–(f) Tunneling spectra measured at marked positions in (a) ($V_{set} = 30$ mV, $I_{set} = 200$ pA). The characteristic peaks are marked by arrows. (g) The statistics of the peak energies derived from 900 spectra which are measured at points with a matrix of 30×30 uniformly distributed in the area of (a) ($V_{set} = 50$ mV, $I_{set} = 500$ pA). All measurements were carried out at 1.7 K.

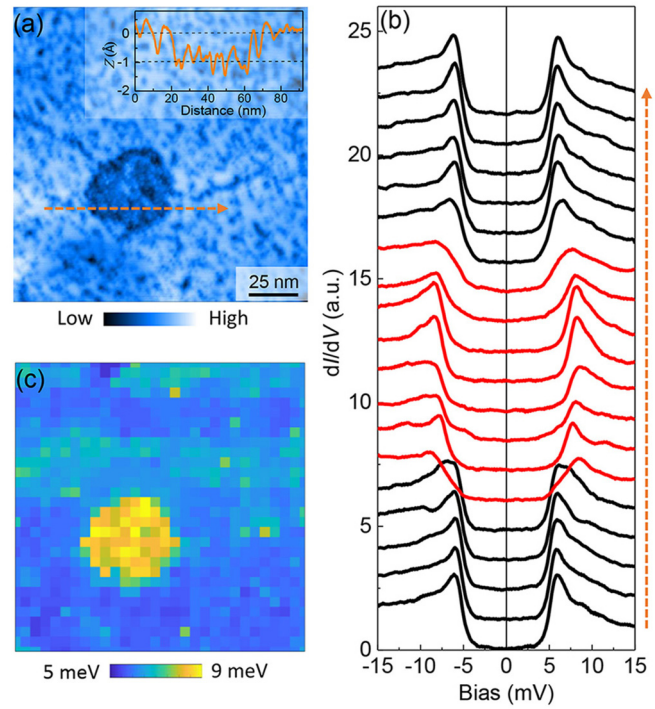

FIG. 8. (a) Topographic image with an exposed low-lying area of the underlayer ($V_{set} = 50$ mV, $I_{set} = 100$ pA). The inset shows the line profile of the surface height along the arrowed line, and the exposed low-lying layer is about 1 Å on average lower than the top surface layer. (b) A set of tunneling spectra measured along the dashed line in (a) ($V_{set} = 50$ mV, $I_{set} = 200$ pA). (c) Color mapping of the coherence peak energy on the positive-bias side based on 900 tunneling spectra measured at points with a matrix of 30×30 uniformly distributed in the area of (a) ($V_{set} = 50$ mV, $I_{set} = 200$ pA). All measurements were carried out at 1.7 K.

IV. DISCUSSION

On the surfaces of $KCa_2Fe_4As_4F_2$ single crystals, we observe the $\sqrt{2}\times\sqrt{2}$ reconstructed layer of atoms. It is consistent with the fact that half of the potassium atoms or calcium atoms of a layer should stay and be reconstructed on each cleaved surface. The reconstruction can lead to electrically unpolar surfaces. It should be noted that there are many hollows that are subnanometer or several nanometers in size randomly distributed on the surface. Such topography with hollows is very common in FeSCs with an exposed surface composed of alkali-metal atoms [23–25]. The hollow population and distribution may be different in a surface terminated by alkaline-earth-metal atoms. In this point of view and considering the observed features, the hollows are either K or Ca vacancies, which may be due to easy loss of these atoms in the cleaving procedure. The missing K/Ca atoms on the surface will adjust the band structure slightly, which is supported by the different features beyond the gap in spectra shown in Figs. 2(b) and 7(b).

We observe an obvious fully gapped feature in most tunneling spectra measured in K12442 single crystals, which indicates the absence of nodes and is consistent with other measurements [14–16]. Most of the coherence peaks locate in the energy range from 4 to 7 meV, and these gap values seem to be comparable to those reported previously [14,16,41]. Since the dominant contribution of the FT-QPI is consistent with the intrapocket scattering of the α pocket, the obtained superconducting gap values on the easily achieved surface are likely to be assigned to this hole pocket. Therefore, the superfluid may be mainly contributed by the holelike Fermi surfaces near the Γ point. The situation is similar to that in $CaKFe_4As_4$: several hole and electron pockets are observed near the Γ and M points by the ARPES measurement [42], but only the scattering between two hole pockets is observed in FT-QPI patterns from the STM measurement [35]. The hump feature at about 8–11 meV observed on the rarely achieved surface in K12442 may be the larger superconducting gap, as reported previously [17], or the bosonic mode corresponding to some gap(s). If it were the bosonic mode, the mode energy should be about 2–6 meV according to the substraction of the superconducting gap energy. However, the measured bosonic

mode value is as large as 16 meV from neutron scattering experiments [20]; thus, this feature most likely reflects an energy gap. In fact, the top surface can be reconstructed by K or Ca atoms, and it is possible that the rarely achieved surface is constructed by atoms different from the commonly obtained surface. The tunneling matrix element may be distinct for STM/STS measurements on these two kinds of surfaces, which may be the reason that we can observe a larger gap with a value from 8 to 11 meV on the rarely observed surface. In addition, clear coherence peaks at about ± 8 meV can be observed on the spectra measured on the lower-lying layer, which confirms the existence of the large superconducting gap in the rarely achieved surface. This gap may open in the holelike β_2 band with a gap value of about 7.8 meV from ARPES measurements [14]. Although we have observed some peaks on the spectra near ± 2.2 mV, due to the existence of some very strong impurity bound states appearing near this energy, we cannot be sure that these features reflect a small superconducting gap [14,17,41]. From our experimental data, the confirmable superconducting gap ranges from 4 to 7 meV, and the dominant contribution of the superfluid may be from the bands with gaps of about 4.4 to 5.4 meV, most likely the hole derivative α band near Γ. However, the determined Fermi energy of the α band is only about 24 ± 6 meV, indicating that the basic requirement of the BCS theory in the weak-coupling limit, namely, $E_F \gg \Delta$, cannot be satisfied in K12442. This strongly suggests that the superconducting physics in the K12442 material should possess by itself an unconventional feature. In addition, the very shallow band and relatively high T_c make the material satisfy the extreme quantum limit, so we can observe discrete vortex bound states with energy levels deviating from the widely believed ratio of $1:3:5$ in K12442 single crystals, which is reported in a separate paper [43].

In FeSCs, the scenario of $s^{\pm}$ pairing is based on the nesting between hole and electron pockets with similar sizes in the weak-coupling scenario. This pairing manner was first inferred from the QPI measurements of Fe(Se,Te) by comparing the difference when the applied magnetic field is zero and finite [30]. It was later further strengthened by the impurity effect [44] and phase-resolved QPI analysis [45]. However, this pairing mechanism is challenged in K12442 because the electron pocket at the M point is too small [14], so the nesting condition cannot be satisfied. In our measurements, we cannot even observe the scattering pattern between the hole pockets and tiny electron pockets in the FT-QPI result. Very different sizes of the hole and electron pockets challenge the nesting picture of $s^{\pm}$ pairing in the weak-coupling scenario. However, from tunneling spectra obtained in this work, if the impurity is nonmagnetic in nature as we argued, the impurity bound states at about ± 2.2 meV may suggest a sign change in the superconducting gaps in this superconductor. According to Anderson's theorem [46,47], nonmagnetic impurities do not break the Cooper pairs in a superconductor with a sign-preserved gap(s), while they are detrimental to superconductivity and can induce clear in-gap bound-state peaks in a superconductor with a sign-reversal gap(s) [48–50]. Therefore, the bound states induced by nonmagnetic impurities may suggest a sign change in superconducting gaps in this superconductor. In any case, it remains unclear but would be interesting to know what role is played by the shallow electron pocket and even the incipient hole bands [14] near the M point and whether they help form the "incipient" $s^{\pm}$ pairing [51].

V. CONCLUSION

In conclusion, using a scanning tunneling microscope, we have investigated the superconducting gaps and pairing mechanism of $KCa_2Fe_4As_4F_2$ single crystals. Most spectra exhibit a full gap feature with a gap value from 4 to 8 meV. On a few spectra, some peaks can be observed at about ± 2.2 meV, which can be attributed to the impurity-induced bound states. We have not seen the characteristic scattering pattern between hole and electron pockets based on the QPI data and related analysis; however, the FT-QPI pattern can be well described by the intrapocket scattering of the α pocket near the Γ point. The dispersion derived from the FT-QPI indicates a small Fermi energy of about 24 meV for the band forming the α pocket. This indicates a strong deviation from the basic requirement of the weak-coupling BCS theory. Our results help to clarify the superconducting mechanism in iron-based superconductors.

ACKNOWLEDGMENTS

We appreciate useful discussions with A. V. Balatsky, Z. Y. Wang, and D. Wang. This work was supported by the National Key R&D Program of China (Grants No. 2016YFA0300401, No. 2018YFA0704200, No. 2017YFA0303100, and No. 2017YFA0302900), the National Natural Science Foundation of China (Grants No. 12061131001, No. 11974171, No. 11822411, No. 11961160699, No. 11674406, and No. 11674372), and the Strategic Priority Research Program (B) of the Chinese Academy of Sciences (Grants No. XDB25000000 and No. XDB33000000). H.L. is grateful for the support from the Beijing Natural Science Foundation (Grant No. JQ19002) and the Youth Innovation Promotion Association of CAS (Grant No. 2016004).

[1] P. J. Hirschfeld, M. M. Korshunov, and I. I. Mazin, Rep. Prog. Phys. **74**, 124508 (2011).

[2] Z. C. Wang, C. Y. He, S. Q. Wu, Z. T. Tang, Y. Liu, A. Ablimit, C. M. Feng, and G. H. Cao, J. Am. Chem. Soc. **138**, 7856 (2016).

[3] Z. C. Wang, C. Y. He, Z. T. Tang, S. Q. Wu, and G. H. Cao, Sci. China Mater. **60**, 83 (2017).

[4] T. Wang, J. Chu, H. Jin, J. Feng, L. Wang, Y. Song, C. Zhang, X. Xu, W. Li, Z. Li, T. Hu, D. Jiang, W. Peng, X. Liu, and G. Mu, J. Phys. Chem. C **123**, 13925 (2019).

[5] Z.-C. Wang, Y. Liu, S.-Q. Wu, Y.-T. Shao, Z. Ren, and G.-H. Cao, Phys. Rev. B **99**, 144501 (2019).

[6] A. B. Yu, T. Wang, Y. F. Wu, Z. Huang, H. Xiao, G. Mu, and T. Hu, Phys. Rev. B **100**, 144505 (2019).

[7] S. Pyon, Y. Kobayashi, A. Takahashi, W. Li, T. Wang, G. Mu, A. Ichinose, T. Kambara, A. Yoshida, and T. Tamegai, Phys. Rev. Mater. **4**, 104801 (2020).

[8] J. Ishida, S. Iimura, and H. Hosono, Phys. Rev. B **96**, 174522 (2017).

[9] X. Yi, M. Li, X. Xing, Y. Meng, C. Zhao, and Z. Shi, New J. Phys. **22**, 073007 (2020).

[10] B. Wang, Z.-C. Wang, K. Ishigaki, K. Matsubayashi, T. Eto, J. Sun, J.-G. Cheng, G.-H. Cao, and Y. Uwatoko, Phys. Rev. B **99**, 014501 (2019).

[11] T. Wang, C. Zhang, L. Xu, J. Wang, S. Jiang, Z. Zhu, Z. Wang, J. Chu, J. Feng, L. Wang, W. Li, T. Hu, X. Liu, and G. Mu, Sci. China Phys. Mech. Astron. **63**, 227412 (2020).

[12] G. T. Wang, Z. W. Wang, and X. B. Shi, Europhys. Lett. **116**, 37003 (2016).

[13] B. Singh and P. Kumar, in *National Conference on Advanced Materials and Nanotechnology - 2018: AMN-2018*, AIP Conf. Proc. No. 2009 (AIP, Melville, NY, 2018), p. 020002.

[14] D. Wu *et al.*, Phys. Rev. B **101**, 224508 (2020).

[15] Y. Y. Huang, Z. C. Wang, Y. J. Yu, J. M. Ni, Q. Li, E. J. Cheng, G. H. Cao, and S. Y. Li, Phys. Rev. B **99**, 020502(R) (2019).

[16] B. Xu, Z. C. Wang, E. Sheveleva, F. Lyzwa, P. Marsik, G. H. Cao, and C. Bernhard, Phys. Rev. B **99**, 125119 (2019).

[17] M. Smidman, F. K. K. Kirschner, D. T. Adroja, A. D. Hillier, F. Lang, Z. C. Wang, G. H. Cao, and S. J. Blundell, Phys. Rev. B **97**, 060509(R) (2018).

[18] F. K. K. Kirschner, D. T. Adroja, Z. C. Wang, F. Lang, M. Smidman, P. J. Baker, G. H. Cao, and S. J. Blundell, Phys. Rev. B **97**, 060506(R) (2018).

[19] T. Wang, J. N. Chu, J. X. Feng, L. L. Wang, X. G. Xu, W. Li, H.-H. Wen, X. S. Liu, and G. Mu, Sci. China Phys. Mech. Astron. **63**, 297412 (2020).

[20] W. Hong, L. Song, B. Liu, Z. Li, Z. Zeng, Y. Li, D. Wu, Q. Sui, T. Xie, S. Danilkin, H. Ghosh, A. Ghosh, J. Hu, L. Zhao, X. Zhou, X. Qiu, S. Li, and H. Luo, Phys. Rev. Lett. **125**, 117002 (2020).

[21] D. T. Adroja, S. J. Blundell, F. Lang, H. Luo, Z.-C. Wang, and G.-H. Cao, J. Phys.: Condens. Matter **32**, 435603 (2020).

[22] P. Dai, J. Hu, and E. Dagotto, Nat. Phys. **8**, 709 (2012).

[23] X. Zhou, P. Cai, A. Wang, W. Ruan, C. Ye, X. Chen, Y. You, Z. Y. Weng, and Y. Wang, Phys. Rev. Lett. **109**, 037002 (2012).

[24] S. Chi, S. Grothe, R. Liang, P. Dosanjh, W. N. Hardy, S. A. Burke, D. A. Bonn, and Y. Pennec, Phys. Rev. Lett. **109**, 087002 (2012).

[25] X. Liu, R. Tao, M. Ren, W. Chen, Q. Yao, T. Wolf, Y. Yan, T. Zhang, and D. Feng, Nat. Commun. **10**, 1039 (2019).

[26] R. C. Dynes, J. P. Garno, G. B. Hertel, and T. P. Orlando, Phys. Rev. Lett. **53**, 2437 (1984).

[27] J. E. Hoffman, Rep. Prog. Phys. **74**, 124513 (2011).

[28] M. P. Allan, A. W. Rost, A. P. Mackenzie, Y. Xie, J. C. Davis, K. Kihou, C. H. Lee, A. Iyo, H. Eisaki, and T.-M. Chuang, Science **336**, 563 (2012).

[29] Z. Y. Du, X. Yang, H. Lin, D. L. Fang, G. Du, J. Xing, H. Yang, X. Y. Zhu, and H.-H. Wen, Nat. Commun. **7**, 10565 (2016).

[30] T. Hanaguri, S. Niitaka, K. Kuroki, and K. Takagi, Science **328**, 474 (2010).

[31] S. Chi, S. Johnston, G. Levy, S. Grothe, R. Szedlak, B. Ludbrook, R. Liang, P. Dosanjh, S. A. Burke, A. Damascelli, D. A. Bonn, W. N. Hardy, and Y. Pennec, Phys. Rev. B **89**, 104522 (2014).

[32] P. O. Sprau, A. Kostin, A. Kreisel, A. E. Böhmer, V. Taufour, P. C. Canfield, S. Mukherjee, P. J. Hirschfeld, B. M. Andersen, and J. C. S. Davis, Science **357**, 75 (2017).

[33] Z. Du, X. Yang, D. Altenfeld, Q. Gu, H. Yang, I. Eremin, P. J. Hirschfeld, I. I. Mazin, H. Lin, X. Zhu, and H.-H. Wen, Nat. Phys. **14**, 134 (2018).

[34] Q. Gu, S. Wan, Q. Tang, Z. Du, H. Yang, Q.-H. Wang, R. Zhong, J. Wen, G. D. Gu, and H.-H. Wen, Nat. Commun. **10**, 1603 (2019).

[35] A. Fente, W. R. Meier, T. Kong, V. G. Kogan, S. L. Bud'ko, P. C. Canfield, I. Guillamón, and H. Suderow, Phys. Rev. B **97**, 134501 (2018).

[36] W. Li, H. Ding, P. Deng, K. Chang, C. Song, K. He, L. Wang, X. Ma, J.-P. Hu, X. Chen, and Q.-K. Xue, Nat. Phys. **8**, 126 (2012).

[37] J.-X. Yin *et al.*, arXiv:2011.07701.

[38] Z. Wang, H. Yang, D. Fang, B. Shen, Q.-H. Wang, L. Shan, C. Zhang, P. Dai, and H.-H. Wen, Nat. Phys. **9**, 42 (2012).

[39] L. Shan, J. Gong, Y.-L. Wang, B. Shen, X. Hou, C. Ren, C. Li, H. Yang, H.-H. Wen, S. Li, and P. Dai, Phys. Rev. Lett. **108**, 227002 (2012).

[40] T. Hanke, S. Sykora, R. Schlegel, D. Baumann, L. Harnagea, S. Wurmehl, M. Daghofer, B. Buchner, J. van den Brink, and C. Hess, Phys. Rev. Lett. **108**, 127001 (2012).

[41] J. Chu, T. Wang, H. Zhang, Y. Liu, J. Feng, Z. Li, D. Jiang, G. Mu, Z. Di, and X. Xie, Chin. Phys. Lett. **37**, 127401 (2020).

[42] D. Mou, T. Kong, W. R. Meier, F. Lochner, L.-L. Wang, Q. Lin, Y. Wu, S. L. Bud'ko, I. Eremin, D. D. Johnson, P. C. Canfield, and A. Kaminski, Phys. Rev. Lett. **117**, 277001 (2016).

[43] X. Chen, W. Duan, X. Fan, W. Hong, K. Chen, H. Yang, S. Li, H. Luo, and H.-H. Wen, Phys. Rev. Lett. **126**, 257002 (2021).

[44] H. Yang, Z. Y. Wang, D. L. Fang, Q. Deng, Q.-H. Wang, Y.-Y. Xiang, Y. Yang, and H.-H. Wen, Nat. Commun. **4**, 2749 (2013).

[45] M. Chen, Q. Tang, X. Chen, Q. Gu, H. Yang, Z. Du, X. Zhu, E. Wang, Q.-H. Wang, and H.-H. Wen, Phys. Rev. B **99**, 014507 (2019).

[46] P. W. Anderson, J. Phys. Chem. Solids **11**, 26 (1959).

[47] A. V. Balatsky, I. Vekhter, and J.-X. Zhu, Rev. Mod. Phys. **78**, 373 (2006).

[48] Y. Bang, H.-Y. Choi, and H. Won, Phys. Rev. B **79**, 054529 (2009).

[49] T. Kariyado and M. Ogata, J. Phys. Soc. Jpn. **79**, 083704 (2010).

[50] A. F. Kemper, C. Cao, P. J. Hirschfeld, and H. P. Cheng, Phys. Rev. B **80**, 104511 (2009).

[51] X. Chen, S. Maiti, A. Linscheid, and P. J. Hirschfeld, Phys. Rev. B **92**, 224514 (2015).